Thinning and flow of Tibetan crust constrained by the seismic anisotropy

Nikolai M. Shapiro[1], Michael H. Ritzwoller[1], Peter Molnar[2], and Vadim Levin[3]
[1]Department of Physics, University of Colorado at Boulder, USA
[2]Department of Geological Sciences, Cooperative Institute for Research in Environmental Science (CIRES), University of Colorado at Boulder, USA
[3]Rutgers University, New Jersey, USA

Intermediate-period Rayleigh and Love waves propagating across Tibet require marked radial anisotropy within the mid-lower crust, consistent with a thinning of it. The anisotropy is largest in the western part of the plateau where the moment tensors of earthquakes indicate active crustal thinning. A preferred orientation of mica crystals resulting from the crustal thinning can account for the observed anisotropy. The observed mid-crustal anisotropy requires a thinning of approximately 30%, much more than what is estimated for the upper crust. This difference suggests that the mid-lower crust of Tibet has thinned more than the upper crust, consistent with deformation of a mechanically weak layer in the mid-lower Tibetan crust that flows as if confined to a channel (1, 2, 3, 4).

Although most of the high terrain and the thick crust of the Tibetan plateau has resulted from India's penetration into Eurasia, east-west extension and crustal thinning dominate the current active deformation in the highest parts of the plateau (5, 6, 7). Two processes may have contributed to this change in deformation: a gain in potential energy per unit area, due to removal of dense mantle material beneath the plateau (8) and a warming and weakening of middle and lower crust (1). These processes are not independent, because conductive warming of Tibetan crust to make it weak is slow, requiring tens of millions of years, unless some other process such as removal of mantle material (9) or frictional heating (10) are involved. Details of the current

deformation at depth beneath Tibet are poorly known, however, and the assumtion that the crust and the mantle beneath Tibet deform coherently as a thin viscous sheet yields simple explanations of many aspects of Asian tectonics (11, 12, 13). This view is supported both by fault plane solutions of intermediate depth earthquakes ($\geq$70 km) from southern Tibet that show the similar east-west extension and normal faulting (14, 15, 16) as the earthquakes in the upper crust and by the correlation between the estimated strain within the crust and the observed shear wave splitting that is believed to reflect the strain in the mantle (17, 18). At the same time, other evidence suggests that the middle crust of Tibet, at least in some regions, is hot, if not partially molten, and hence very weak (19, 20). Thus, crustal thinning might be dominated by, if not confined to, a flow in the mid to lower crust (1, 2, 3, 4). As we discuss below, the crustal thinning can manifest itself by preferential reorientation of mica crystals into the horizontal plane, which will result in radial anisotropy with horizontally polarized shear waves propagating faster than those vertically polarized.

Using Love and Rayleigh waves, which are horizontally and vertically polarized respectively, we show such radial anisotropy within the middle and lower crust. Rayleigh waves crossing Tibet are characterized by a strong inverse dispersion at periods between 20 and 40 s, whereas dispersion of Love waves at those periods remains near normal (Fig. 1). A seismically isotropic crust cannot fit simultaneously the observed Rayleigh and Love wave group-velocity dispersion curves (Figs. 2a-b). This intermediate-period Rayleigh-Love discrepancy requires the presence of a strong radial anisotropy in the middle Tibetan crust. To study the extent of this feature, we combined more than 45,000 crossing surface wave paths (21) (Fig. SM1) with published phase velocity measurements (22, 23) to constrain the 3D shear velocity structure of the Tibetan crust and uppermost mantle. Because long propagation paths do not allow tight lateral resolution, we added more than 2,500 group-velocity dispersion measurements from portable broadband seismic stations installed within and in vicinity of Tibet (24).

We follow a two-step inversion procedure. First, we use the surface-wave diffraction

tomography (25) to construct dispersion maps at various periods varying between 18-200 s and between 40-150 s for group and phase velocities, respectively. Then, we use the Monte-Carlo method (26) to invert the regionalized dispersion curves for the shear velocity structure of the crust and the uppermost mantle on a $1^\circ \times 1^\circ$ grid across the region of study. Results of the inversion show that the observed dispersion curves require the presence of a strong radial anisotropy in the middle Tibetan crust (Figs. 2c-d, Table SM1). Previous surface-wave studies in Tibet (9, 27, 28, 29, 30, 31) have not detected this crustal anisotropy either because they were based on too few data or they used only Rayleigh waves. Analyses of teleseismic receiver functions (32, 33), however, confirm the anisotropic character of the Tibetan crust.

The mid-crustal radial anisotropy stands out most clearly beneath the high plateau between 80°E and 95°E (Fig. 2e). Because of limited vertical resolution of surface waves, we can not determine the exact depth extent and magnitude of the radial anisotropy but prefer to show its vertically averaged strength represented by the corresponding travel time difference between SV and SH waves, if they propagated vertically through the middle crust. Similarly, because of the limited horizontal resolution of the tomogram, we ignore minor details of the distribution and concentrate on robust features based on ensembles of acceptable structures, which we estimated from the Monte-Carlo inversion (26). For each geographical location, in addition to the best-fitting structure, we can determine the one with minimal amount of crustal anisotropy (Fig. 2f). In some areas where the best-fitting structure indicates significant anisotropy, the data can be also explained with nearly isotropic models. Only beneath the high plateau, do the observed dispersion curves require strong anisotropy. Therefore, we interpret the mid-crustal anisotropy only from this part of Tibet, and we estimate the average $t_{SV} - t_{SH}$ travel-time difference from this area to be 0.5 ± 0.18s.

It has been suggested that mica can play the most important role in the formation of mid-lower crustal anisotropy (34, 35, 36), because of its strongly anisotropic behavior; the shear moduli for shear waves polarized parallel to the plane of mica

crystals are larger than those for polarization perpendicular to them (37). Thus, a near-horizontal orientation of mica crystals will produce the radial anisotropy. Two different deformation mechanisms of the middle Tibetan crust could result in a preferred horizontal orientation of mica. First, the strong shearing during the underthrusting of the Indian crust beneath Tibet (39) might realign such crystals. Second, the mica crystals can become oriented near-horizontally as a result of the currently occurring crustal thinning. The observed lateral distribution of the radial crustal anisotropy can help to discriminate between these mechanisms. If the thick Tibetan crust was created by the large-scale underthrusting, and this underthrusting was responsible for the radial anisotropy, we would expect the strong radial anisotropy to be observed over nearly the whole plateau where the crust is thick. In the second case, however, if the anisotropy resulted from the crustal thinning, it would be most pronounced where that thinning occurs.

Slip on faults during earthquakes provides an image of current deformation within Tibet (Fig. 3a). The relatively low strain rate in Tibet ($\sim 10^{-8}$/year) (40) and the short duration for which earthquakes can be studied prevent the observed seismicity from providing more than an approximate representation of the crustal straining. Therefore, we use a simple approach to deduce the current deformation regime and exploit only the sign of one component of the moment tensor (41), M_{rr}, which measures the extent to which the slip during an earthquake contributes to the crustal thinning or thickening. The distribution of M_{rr} for earthquakes shallower than 40 km (Fig. 3b) shows the crustal thinning in the same regions where we found the mid-crustal radial anisotropy (Fig. 2f).

This correspondence suggests that the crustal thinning and the rotation of mica crystals into a preferred horizontal alignment (Fig. 4a) makes the mid-lower crust of Tibet anisotropic. To quantify the relation between the crustal thinning and the resulting crustal anisotropy, we estimated the strength of the radial anisotropy in deformed rock aggregates containing 30% of mica embedded into an isotropic matrix.

We considered the simplest case of radially symmetric flattening (Fig. 4b) when the rotation of mica crystals results in an isotropic system with a vertical axis of symmetry, i.e., in a radial anisotropy with $V_{SH} > V_{SV}$. We used laboratory measurements of elastic constants of mica (37) and the Voigt-Reuss-Hill averaging scheme to estimate the elastic tensor and the shear wave speeds of the deformed aggregate (Fig. 4c) (38). The difference between SV and SH travel times depends on the thickness of the anisotropic layer, which is constrained only approximately by the surface-wave inversion. Our results indicate that the anisotropy is definitely required in the middle crust but we cannot exclude the possibility if the anisotropic layer also extends to the lower crust. If the anisotropic layer was limited to the middle crust, its thickness would be about 25-30 km but it might be as thick as 50 km, if the lower crust was also included. Depending on the assumed thickness of the anisotropic layer, between 20% and 40% of vertical flattening strain would be required to produce the observed radial anisotropy in a rock containing 30% mica. This is larger than the amount of the crustal thinning estimated for the Tibetan upper crust($\sim$10%, obtained from an average strain rate of 10^{-8} per year acting for 10 million years). The difference may indicate that the Tibetan middle crust is sufficiently weaker than the upper crust and upper mantle, so that thinning has been concentrated in only part of the crust. This supports the idea that "channel flow" occurs within the Tibetan mid-lower crust (1, 2, 3, 4).

Competing interests statement.

The authors declare that they have no competing financial interests.

References

1. P. Bird, *J. Geophys. Res.* **96**, 10,275-10,286 (1991).

2. L.H. Royden, B.C. Burchfield, R.W. King, E. Wang, Z. Chen, F. Shen, F., Y. Liu, *Science* **276**, 788-790 (1997).

3. M.K. Clark, L.H. Royden, *Geology* **28**, 703-706 (2000).

4. C. Beaumont, R.A. Jamieson, M.H. Nguyen, B. Lee, *Nature* **414**, 738-742 (2001).

5. P. Molnar, P. Tapponnier, *J. Geophys. R.* **83**, 5361-5375 (1978).

6. R. Armijo, P. Tapponnier, J. L. Mercier, T. Han, *J. Geophys. Res.* **91**, 13,803-13,872 (1986).

7. P. Molnar, H. Lyon-Caen, *Geophys. J. Int.* **99**, 123-153 (1989).

8. P.C. England, G.A. Houseman, *J. Geophys. Res.* **94**, 17,561-17,579 (1989).

9. W.-P. Chen, P. Molnar, *J. Geophys. Res.* **86**, 5937-5962 (1981).

10. C. Kincaid, P. Silver, *Earth and Planet. Sci. Lett.* **142**, 271-288 (1996).

11. P. England, G. Houseman, *J. Geophys. Res.* **91**, 3664-3676 (1986).

12. P. England, P. Molnar, *Science* **278**, 647-650 (1997).

13. L.M. Flesch, A.J. Haines, W.E. Holt, *J. Geophys. Res.* **106**, 16,435-16,460 (2001).

14. W.-P. Chen, J. L. Nabelek, T. J. Fitch, P. Molnar, *J. Geophys. Res.* **86**, 2863-2876 (1981).

15. P. Molnar, W.-P. Chen, *J. Geophys. Res.* **88**, 1180-1196 (1983).

16. L. Zhu, and D. V. Helmberger, *Geophys. Res. Lett.* **23**, 435-438 (1996).

17. P. Davis, P. England, G. Houseman, *J. Geophys. R.* **102**, 27,511-27,522 (1997).

18. W.E. Holt, *Geology* **28**, 67-70 (2000).

19. K.D. Nelson et al., *Science* **274**, 1684-1688 (1996).

20. Y. Makovsky, S.L. Klemperer, *J. Geophys. R.* **104**, 10795-10825 (1999).

21. M.H. Ritzwoller, A.L. Levshin, *J. Geophys. Res.* **103**, 4839-4878 (1998).

22. J. Trampert, J.H. Woodhouse, *Geophys. J. Int.* **122**, 675-690 (1995)

23. G. Ekström, J. Tromp, E.W.F. Larson, *J. Geophys. Res.* **102**, 8137-8157 (1997).

24. We used data from the Tibetan Plateau , INDEPTH-3, the Tien Shan (Roecker et al.), and Himalayan Nepal Tibet Experiment (HIMNT) (Sheehan, Wu et al.) PASSCAL deployments.

25. M.H. Ritzwoller, N.M. Shapiro, M.P. Barmin, A.L. Levshin, *J. Geophys. Res.* **107**, 2335, doi:10.1029/2002JB001777 (2002).

26. N.M. Shapiro, M.H. Ritzwoller, *Geophys. J. Int.* **151**, 88-105 (2002).

27. K.-Y. Chun, T.V. McEvilly, *J. Geophys. Res.* **91**, 10,405-10,411 (1986).

28. N. Cotte, H. Pedersen, M. Campillo, J. Mars, J.F. Ni, R. Kind, E. Sandvol, W. Zhao, *Geophys. J. Int.* **138**, 809-819 (1999).

29. W. Friederich, *Geophys. J. Int.* **153**, 88-102 (2003).

30. Z. Huang, W. Su, Y. Peng, Y. Zheng, H. Li, *J. Geophys. Res.* **108**, 2073, doi:10.1029/2001JB0011696 (2003).

31. R. Rapine, F. Tilmann, M. West, J. Ni, A. Rodgers, *J. Geophys. Res.* **108**, 2120, doi:10.1029/2001JB000445 (2003).

32. H. F. Sherrington, G. Zandt, A. Frederiksen, *J. Geophys. Res.* **109**, B02312, 10.1029/2002JB002345 (2004).

33. N.M. Shapiro, V. Levin. M.H. Ritzwoller, P. Molnar, D. Smith, *Eos Trans. AGU* **84(46)**, Fall Meet. Suppl., Abstract S11C-0307 (2003).

34. T.Weiss, S. Siegesmund, W. Rabbel, T. Bohlen, M. Pohl, *PAGEOPH* **156**, 97-122 (1999).

35. O. Nishizawa, T. Yoshitno, *Geophys. J. Int.* **145**, 19-32 (2001).

36. A. Meltzer, N. Christensen, *Geophys. Res. Lett.* **28**, 2129-2132 (2001).

37. K.S. Aleksandrov, T.V. Ryzhova, *Izv. Acad. Sci. USSR, Geophys. Ser.* **12**, 186-189 (1961).

38. Details of the computations are presented in supporting online material.

39. M. Barazangi, J. Ni, *Geology* **10**, 179-185 (1982).

40. P. Molnar, P. England, J. Martinod, *Geophysics* **31**, 357-396 (1993).

41. We used the CMT catalog available on the Harvard website: http://www.seismology.harvard.edu/CMTsearch.html

42. Most of the data used in this work were obtained from the IRIS Data Management Center and the GEOSCOPE Data Center. We are also particularly grateful to Jeannot Trampert at Utrecht University and Michael Antolik, Adam Dziewonski, and Goran Ekström at Harvard University for providing phase speed measurements and to Anne Sheehan and Francis Wu for providing the HIMNT data. We thank Anatoli Levshin and Abir van Hunen for help in preparing the data set and Philip England and Craig Jones for helpful discussions. This work was supported by NSF grant EAR-0337622.

Received _____

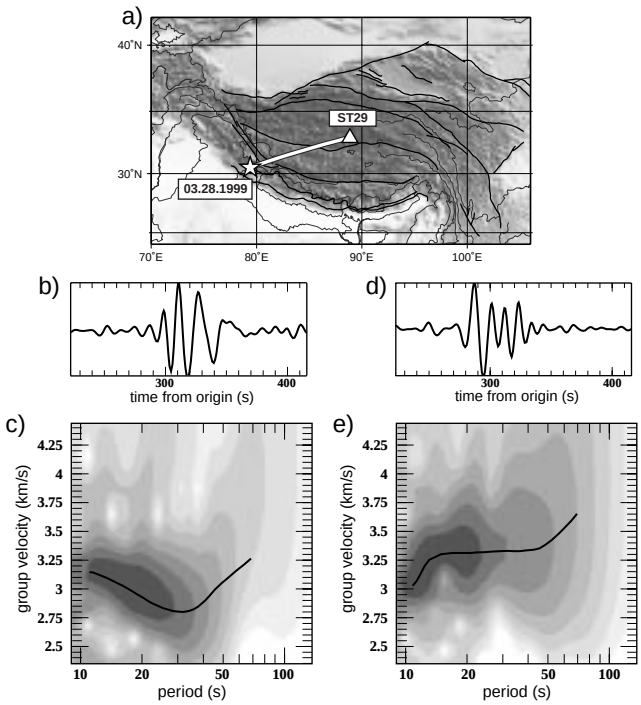

Figure 1. Discrepancy between dispersions of intermediate-period Rayleigh and Love waves across Tibet. (a) Map showing event-station location. (b) Vertical-component (Rayleigh wave) seismogram bandpassed between 15 and 100 s. (c) Vertical-component frequency-time diagram. (d) Transverse-component (Love wave) seismogram bandpassed between 15 and 100 s. (e) Transverse-component frequency-time diagram. Black lines on (c) and (e) show the inferred group-velocity dispersion curves.

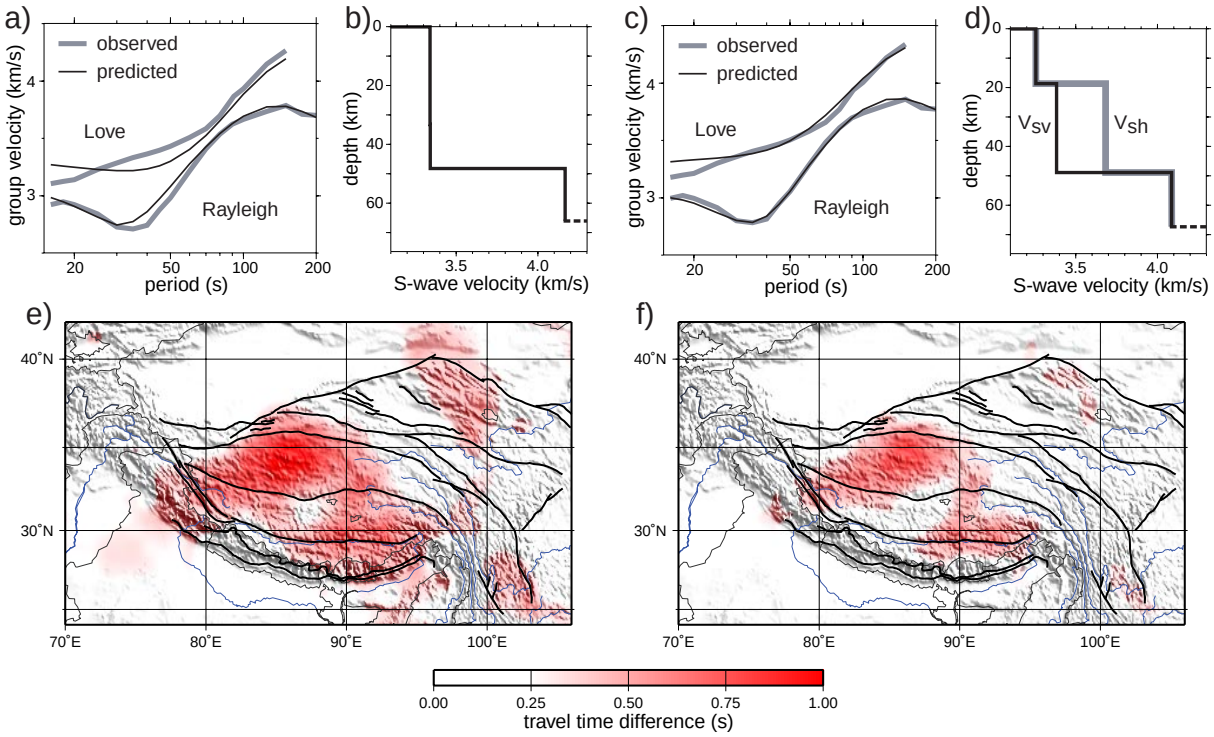

Figure 2. Constraints on seismic wave speeds in the Tibetan crust. (a)-(d) Surface-wave dispersion inversion in a knot of $1^\circ \times 1^\circ$ grid located at 34N, 84E in the western Tibet. (a) Fit of dispersion curves with the isotropic and monotonic parameterization of the crustal structure in (b). (c) Fit with a structure, in (d), that includes radial anisotropy in the middle crust. In (a) and (c), observed (thick gray line) and predicted (thin black line) group velocity dispersion curves correspond to best-fitting crustal structures in (b) and (d). The Moho is shown with the dashed line. (e) Strength of radial anisotropy in the middle crust estimated from the best-fitting structure, represented as the idealized travel time difference between SV and SH propagating vertically through the middle crust. (f) Minimum strength of radial anisotropy required to explain the surface-wave dispersion data.

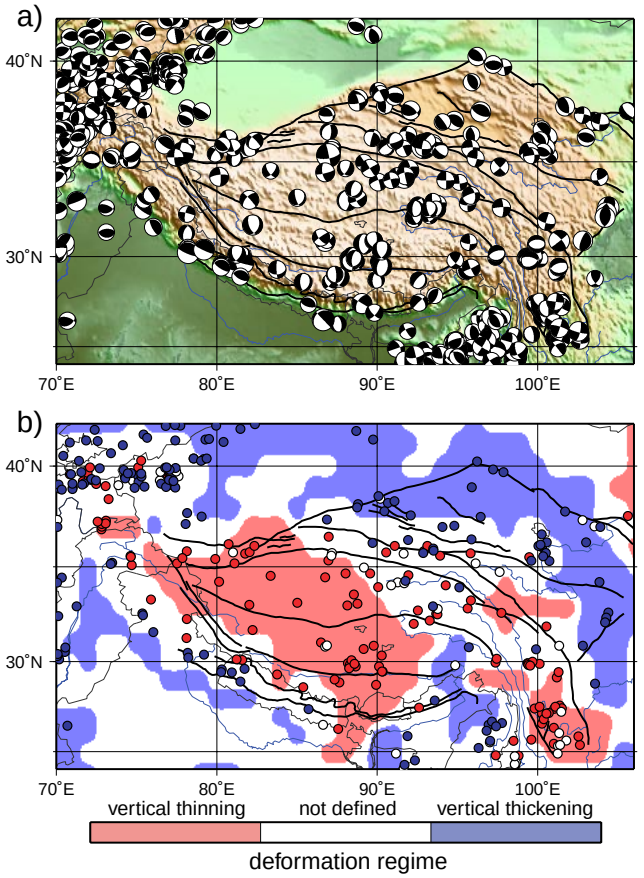

Figure 3. Seismicity of the Tibetan region. (a) Double-couple components of Harvard CMT solutions for the Tibetan region (1973-present). (b) Distribution of the normalized $\tilde{M}_{rr}$ component of the moment tensors ($\tilde{M}_{rr} = M_{rr}/max(M_{rr}, M_{tt}, M_{pp})$). Earthquakes contributing to crustal thinning ($\tilde{M}_{rr} \leq -0.15$) are shown with red circles. Those corresponding to the crustal thickening ($\tilde{M}_{rr} \geq 0.15$) are shown with the blue circles. White circles denote earthquakes small magnitudes of $\tilde{M}_{rr}$. Light red shading shows areas where earthquakes with $\tilde{M}_{rr} \leq -0.15$ are detected within a 200 km radius and no earthquakes with $\tilde{M}_{rr} \geq 0.15$ are detected in the same area. Light blue shading shows the same for $\tilde{M}_{rr} \geq 0.15$ and no events with $\tilde{M}_{rr} \leq -0.15$.

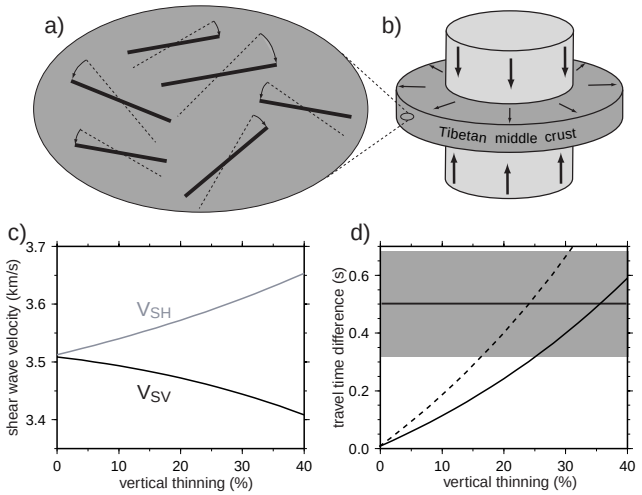

Figure 4. Proposed relationship between the observed mid-crustal radial anisotropy and the ongoing deformation of the Tibetan crust. (a) Thinning of the middle crust causes mica crystals to rotate into horizontal orientations, which results in an anisotropic system with hexagonal symmetry about a vertical axis (b) and different speeds of V_{SV} and V_{SH}. (c) V_{SV} and V_{SH} computed for an aggregate containing 15% biotite, 15% muscovite, and 70% isotropic matrix as function of the flattening strain. (d) Travel time difference between SV and SH propagating through deformed layers with thicknesses of 30 (solid line) and 50 km (dashed line). Horizontal line and shaded area indicate the average travel time difference and its standard deviation estimated for the western Tibet from surface dispersion

Supporting Online Material

Thinning and flow of Tibetan crust constrained by the seismic anisotropy

Nikolai M. Shapiro[1], Michael H. Ritzwoller[1], Peter Molnar[2], and Vadim Levin[3]

[1]Department of Physics, University of Colorado at Boulder, USA

[2]Department of Geological Sciences, Cooperative Institute for Research in Environmental Science (CIRES), University of Colorado at Boulder, USA

[3]Rutgers University, New Jersey, USA

Data coverage and resolution

Surface-wave coverage for the Tibetan region (Fig. SM1) is denser at intermediate periods (~40 sec) than at longer periods. Intermediate periods are most sensitive to the Tibetan middle crustal structure. The average lateral resolution of the group velocity tomographic maps across the Tibetan region at those periods is about 200 km for both Rayleigh and Love waves.

Finding an optimal parameterization of the Tibetan crustal structure

When inverting the surface-wave dispersion maps for the 3D shear velocity model we tested five different parameterizations of the Tibetan crustal structure: two isotropic and three radially anisotropic. During those tests, we set the mantle structure to that obtained from a global inversion (1). Results of those five inversions (Table SM1) show that the parameterization with a radially anisotropic middle crust yields a root-mean-square misfit that is nearly half that of the other parameterizations. Therefore, even if we cannot eliminate a small amount anisotropy in either the upper or the lower crust, we conclude that a strong mid-crustal radial anisotropy is required to explain the observed surface-wave dispersion. During the final inversion, we selected the parameterization with a radially anisotropic middle crust allowed the mantle structure to vary.

Relation between the crustal thinning and the radial anisotropy

We consider a horizontally isotropic crust flattened in its vertical dimension using the strain tensor given by:

$$U = \begin{pmatrix} 1+\frac{\epsilon}{2} & 0 & 0 \\ 0 & 1+\frac{\epsilon}{2} & 0 \\ 0 & 0 & 1-\epsilon \end{pmatrix} \quad (1)$$

where ϵ is the amount of the crustal thinning. We consider a rock composed of mica crystals embedded into an isotropic matrix. In response to the vertical flattening, the mica crystals rotate and become oriented more horizontally. Rotation of an individual mica crystal relative to the vertical axis can be considered as a two-dimensional problem where the crystal is represented by a linear element $\bar{r}$ and its deformation can be written as:

$$\bar{r}' = \begin{pmatrix} 1+\frac{\epsilon}{2} & 0 \\ 0 & 1-\epsilon \end{pmatrix} \bar{r} \tag{2}$$

where $\bar{r}$ and $\bar{r}'$ are its initial and final orientations, respectively. They can be written as:

$$r_x = |\bar{r}|cos\theta \qquad r_z = |\bar{r}|sin\theta \qquad r'_x = |\bar{r}'|cos\theta' \qquad r'_z = |\bar{r}'|sin\theta' \tag{3}$$

where θ and θ' are initial and final angles between the crystal plane and the horizontal. Combining (2) and (3) we obtain:

$$\theta' = arctan\left(\frac{1-\epsilon}{1+0.5\epsilon} tan\theta\right) \tag{4}$$

Those equations govern the rotations of mica crystals in response to vertical flattening.

Mica-group minerals are monoclinic (Table SM2), but their symmetry system can be treated as approximately hexagonal (2,3). For crystals with arbitrary orientations, the elastic tensor $c(\theta, \phi)$ can be computed by applying simple transformations of the fourth-order tensors:

$$c'_{nmop} = \beta_{ni}\beta_{mj}\beta_{ol}\beta_{pk}c_{ijlk} \tag{5}$$

where β is a rotation matrix.

We consider an initial system with an isotropic orientation of mica crystals and apply transformation (4) to it. Resulting Voigt and Reuss averages of the elastic tensor become:

$$c_{voigt}(\epsilon) = \frac{1}{2\pi}\int_0^{2\pi}\int_0^{\pi/2} c\left(arctan\left(\frac{1-\epsilon}{1+0.5\epsilon} tan\theta\right), \phi\right) sin\theta d\theta d\phi \tag{6}$$

$$c^{-1}_{reuss}(\epsilon) = \frac{1}{2\pi}\int_0^{2\pi}\int_0^{\pi/2} c^{-1}\left(arctan\left(\frac{1-\epsilon}{1+0.5\epsilon} tan\theta\right), \phi\right) sin\theta d\theta d\phi \tag{7}$$

We solved equations (6) and (7) numerically for biotite and muscovite and, then, estimated Voigt and Reuss averages in a deformed aggregate composed of biotite and muscovite embedded into an isotropic matrix:

$$c_{voigt}(\epsilon) = a^{bio}c^{bio}_{voigt}(\epsilon) + a^{musc}c^{musc}_{voigt}(\epsilon) + a^{iso}c^{iso} \tag{8}$$

$$c^{-1}_{reuss}(\epsilon) = a^{bio}[c^{bio}_{reuss}(\epsilon)]^{-1} + a^{musc}[c^{musc}_{reuss}(\epsilon)]^{-1} + a^{iso}[c^{iso}]^{-1} \tag{9}$$

where a^{bio}, a^{musc}, and a^{iso} are volumetric fractions for biotite, muscovite and the isotropic matrix, respectively. Finally, we formed the Voigt-Russ-Hill average:

$$c(\epsilon) = \frac{1}{2}(c_{voigt}(\epsilon) + c_{reuss}(\epsilon)) \tag{10}$$

and used it to compute two shear wave velocities:

$$V_{SV}(\epsilon) = \sqrt{\frac{c_{2323}(\epsilon)}{\rho}} \tag{11}$$

$$V_{SH}(\epsilon) = \sqrt{\frac{c_{1212}(\epsilon)}{\rho}} \tag{12}$$

where ρ is density. We use $\rho = 2850$ kg/m^3 and $\mu^{iso} = 42$ GPa.

References

1. N.M. Shapiro, M.H. Ritzwoller, *Geophys. J. Int.* **151**, 88-105 (2002).
2. K.S. Aleksandrov, T.V. Ryzhova, *Izv. Acad. Sci. USSR, Geophys. Ser.* **12**, 186-189 (1961).
3. O. Nishizawa, T. Yoshitno, *Geophys. J. Int.* **145**, 19-32 (2001).

Name	Monotonic constraint	P-to-S ratio	Parameters	Average misfit (m/s)
Isotropic monotonic	Yes	free	v_s^U, v_s^M, v_s^L, v_p^U, v_p^M, v_p^L	66.05
Isotropic	No	free	v_s^U, v_s^M, v_s^L, v_p^U, v_p^M, v_p^L	62.55
Anisotropic upper crust	Yes for isotropic v_s	fixed	v_s^M, v_s^L, v_{sv}^U, v_{sh}^U	57.25
Anisotropic middle crust	Yes for isotropic v_s	fixed	v_s^U, v_s^L, v_{sv}^M, v_{sh}^M	32.78
Anisotropic lower crust	Yes for isotropic v_s	fixed	v_s^U, v_s^M, v_{sv}^L, v_{sh}^L	52.83

Table SM1. Parameterizations of the Tibetan crust tested in this paper. Last column shows the average group velocity misfit at periods below 50 s computed across the Tibetan region (in a square [28N, 76E; 38N, 102E]). Superscripts ^{U}, ^{M}, and ^{L} denote upper-crustal, mid-crustal, and lower-crustal values, respectively.

Mineral	c_{1111}	c_{3333}	c_{2323}	c_{1212}	c_{1133}
biotite	186.0	54.0	5.8	76.8	11.6
muscovite	178.0	54.9	12.2	67.8	14.5

Table SM2. Elastic constants for minerals of the mica group (units are GPa).

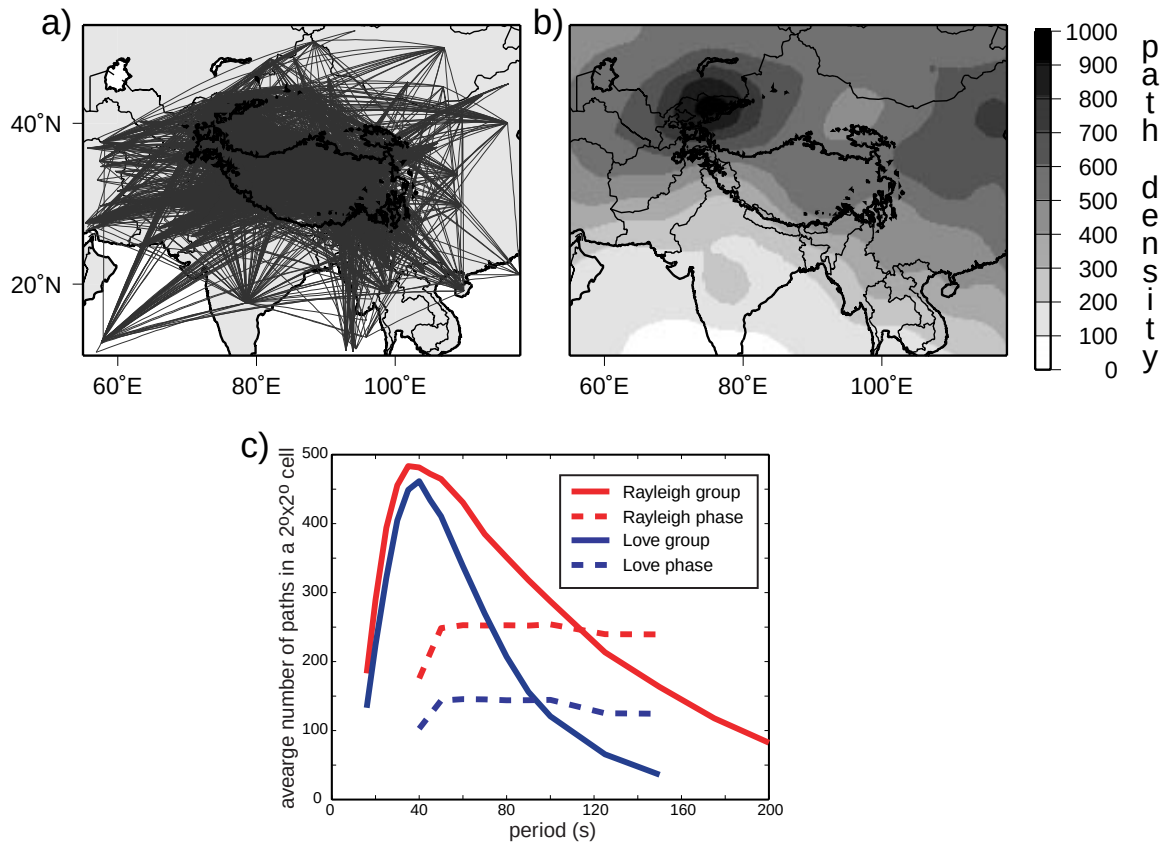

Figure SM1. Surface wave coverage. (a) Regional paths: approximately 3,000 regional surface-wave paths for which we measured dispersion curves for periods $sim40$ s begin and end within the map shown. (b) Total path density (regional + teleseismic paths): more than 45,000 surface wave rays traverse parts of this region. Path density (number of rays crossing each $2^\circ \times 2^\circ$ cell). (c) Path density as a function of period for group and phase speeds of Love and Rayleigh Waves